Biointerface Research in Applied Chemistry
Open-Access Journal (ISSN: 2069-5837)

Article
Volume 14, Issue 4, 2024, 77
https://doi.org/10.33263/BRIAC144.077

Studies on Photocatalytic Degradation of Phenol Red over $CaFe_2O_5$ and $CaFe_2O_5$-TiO_2 nanocomposite

Tejaswini Mendke [1], Chilukoti Srilakshmi [1,*], Thangavel Thirunavukkarasu [1], Partha Partim Das [1]

[1.] Advanced Materials Synthesis Research Lab (AMSRL), GITAM School of Science GITAM (Deemed to be University), Nagadenahalli, Doddaballapur Taluk, Bengaluru, Karnataka 562163
* Correspondence: schiluko@gitam.edu;

Scopus Author ID 9240218200
Received: 10.12.2023; Accepted: 8.04.2024; Published: 19.07.2024

Abstract: In this study, $Ca_2Fe_2O_5$ and $Ca_2Fe_2O_5$-TiO_2 nanomaterials were synthesized using a microwave-assisted hydrothermal synthesis method, followed by calcination at 900°C for 10 hours. The materials were characterized using Fourier-transform infrared spectroscopy (FT-IR), powder X-ray diffraction (XRD), and scanning electron microscopy (SEM). The band gap energy (Eg) of $Ca_2Fe_2O_5$ and $Ca_2Fe_2O_5$-TiO_2 was determined to be approximately 2.48 and 3.64 eV, respectively. Including the TiO_2 component resulted in a significant increase of 1.16 eV in the band gap energy of $Ca_2Fe_2O_5$-TiO_2 compared to $Ca_2Fe_2O_5$. TEM analysis showed that $Ca_2Fe_2O_5$ exhibits a flake-like morphology, while $Ca_2Fe_2O_5$-TiO_2 showed a mixed morphology with TiO_2 nanoparticles dispersed on the flakes of $Ca_2Fe_2O_5$. The photocatalytic activity of the materials was evaluated for phenol red dye degradation in aqueous solutions having concentrations from 10 to 1000 ppm, and it found that the UV/H_2O_2/$Ca_2Fe_2O_5$-TiO_2 system had superior degradation efficiency compared to the UV/H_2O_2/$Ca_2Fe_2O_5$ system, particularly at high dye concentrations. The photocatalytic data for both $Ca_2Fe_2O_5$ and $Ca_2Fe_2O_5$-TiO_2 followed first-order kinetics. The present study suggests that $Ca_2Fe_2O_5$-TiO_2 could be a cost-effective material for efficiently removing dyes from industrial wastewater. The findings contribute to the potential application of these nanomaterials in environmental remediation and water treatment processes.

Keywords: $Ca_2Fe_2O_5$-TiO_2; photocatalytic degradation; phenol red.

1. Introduction

Heterogeneous photocatalysis is a crucial technique for effectively removing pollutants from liquids and gases using nanocrystalline semiconductors. To achieve successful pollutant removal, nanomaterials with sufficient surface area and appropriate physical properties that facilitate the handling of light-triggered charge carriers and enable them to participate in chemical reactions at the catalyst surface are essential [1-4]. In this context, perovskite-type transition metal oxides (ABO_3 structure) have garnered considerable attention as catalytic materials owing to their thermal and chemical stability, resistance to dissolution in both aqueous and nonaqueous solutions, and cost-effectiveness relative to noble metals [5]. Various compounds like $NaBiO_3$, $LaMnO_3$, $NiTiO_3$, $BaTiO_3$, $BiFeO_3$, and $LaFeO_3$ [6-13] have been utilized for photocatalytic degradation of dyes due to their stable perovskite structure. Combining perovskite with other metal oxide components in composite form has garnered importance due to the synergistic effect between the two materials. Composite systems offer

numerous advantages, including surface modification and improved optical and charge-handling properties compared to individual compounds like TiO_2, often used as a reference material for photocatalytic behavior. Hence, designing and developing distinct TiO_2-based nanocomposites is crucial for environmental applications [14-16]. These composite systems with TiO_2 have proven to be effective catalysts for dye degradation and redox photo reactions, demonstrating their potential for practical use in environmental remediation [17-20].

Dyes are recognized as significant pollutants in wastewater due to their high toxicity and potential to accumulate in the environment. Various industries, including paper, textile, cosmetics, food, pharmaceutical, and plastic, discharge effluents containing highly colored contents into nearby water bodies, causing water pollution [21]. These colored effluents, especially dyes, pose serious environmental, aesthetic, and health problems as they are carcinogenic and toxic to humans and aquatic organisms [22-25]. One example is phenol red, a water-soluble textile dye used as a pH indicator. Although it is employed in cell biology studies and water testing applications, phenol red's toxic effects include eye, respiratory, and skin irritation and inhibiting renal epithelial cell growth. It also exhibits adverse effects on muscle fibers and has been reported to be mutagenic. Due to its toxicity, there is an urgent need for cost-effective techniques to remove dyes from wastewater. Thus, this research focuses on photocatalytic degradation as the most effective method for removing phenol red from aqueous solutions, aiming to develop an environmentally friendly and efficient approach for dye removal [26-31].

Previous research has extensively studied the Fenton reagent as a highly effective method for removing dyes and organic pollutants from water through a photocatalytic route[32,33]. Building on these findings, our current study focuses on synthesizing a Fe-based ternary perovskite, specifically $Ca_2Fe_2O_5$, and a composite of this compound with TiO_2, denoted as $Ca_2Fe_2O_5$-TiO_2, for the photocatalytic degradation of phenol red. Both compounds were synthesized using a microwave-assisted hydrothermal method, which offers advantages such as rapid crystallization, cost efficiency, clean technology, energy efficiency, and low cost. To the best of our knowledge, this is the first report evaluating the photocatalytic activity of the perovskite $Ca_2Fe_2O_5$ and the $Ca_2Fe_2O_5$-TiO_2 composite in the degradation of phenol red under UV irradiation in the presence of H_2O_2. The catalysts were characterized using techniques like powder X-ray diffraction (XRD), Fourier transform infrared (FTIR) spectroscopy, field emission scanning electron microscopy (FESEM), and UV-visible absorption spectroscopy. These characterizations provide valuable insights into the structure and properties of the synthesized materials, aiding in the understanding of their photocatalytic performance for phenol red degradation.

2. Materials and Methods

2.1. Materials.

$Fe(NO_3)_3{\cdot}9H_2O$ (98 %) and TiO_2 (99.8 %) were obtained from Merck. Hydrogen peroxide (30 %), potassium hydroxide, Calcium chloride, and phenol red were obtained from SD Fine Chemicals Ltd. The reagents were used as received.

2.2. Synthesis of $Ca_2Fe_2O_5$ by microwave-assisted hydrothermal method.

In the microwave-assisted hydrothermal method, calcium chloride, iron nitrate, and potassium hydroxide are starting materials in a molar ratio 1:1:30 for $CaCl_2$: $Fe(NO_3)_3{\cdot}9H_2O$:

KOH. First, $CaCl_2$ and $Fe(NO_3)_3 \cdot 9H_2O$ were separately dissolved in the appropriate amount of deionized water, and both solutions were stirred. Then, the KOH aqueous solution was added drop by drop to the homogeneous solution until precipitation was complete. A dark brown precipitate was formed during this process, and the mixture was stirred for an hour. The resulting solution was transferred to a Teflon-lined autoclave, which was then sealed and placed in a microwave instrument (MW 5000, SINEO, maximum power of 1500 W) and heated to 180°C for 1.5 hours. Afterward, the autoclave was allowed to cool to room temperature, and the solid product, $Ca_2Fe_2O_5$, was washed several times with a 0.1 M aqueous acetic acid solution and then with deionized water, as shown in Figure 1. The $Ca_2Fe_2O_5$ product thus obtained was filtered, dried in a hot air oven at 105°C overnight, and calcined in a muffle furnace at 900°C for 10 hours.

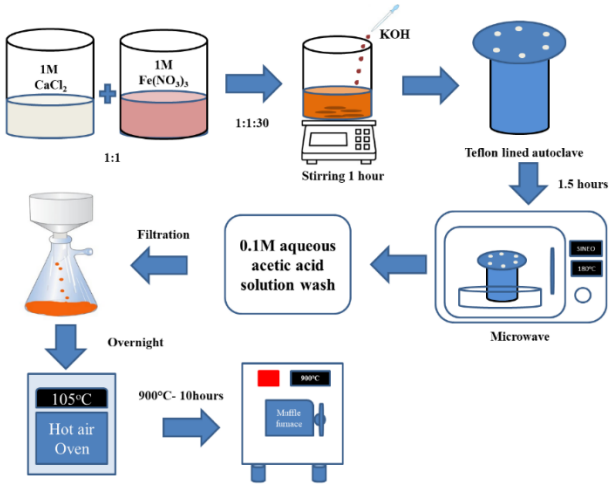

Figure 1. Schematic description of the material synthesis.

2.3. Synthesis of $Ca_2Fe_2O_5$-TiO_2.

The preparation of $Ca_2Fe_2O_5$-TiO_2 followed a similar procedure as described in section 2.2. However, in this case, 0.4 g of TiO_2 was added to the solution containing $CaCl_2$, Fe $(NO_3)_3 \cdot 9H_2O$, and KOH to create the composite material. The resulting mixture was stirred and processed as before, leading to the formation of $Ca_2Fe_2O_5$-TiO_2. The final product was filtered, dried in a hot air oven at 105°C overnight, and then calcined at 900°C for 10 hours to obtain the composite material.

2.4. Characterization of catalysts.

All the catalysts were characterized by various analytical techniques: Powder X-ray diffraction (XRD) was measured using PAN analytical X'pert PRO Powder Diffractometer with Cu Kα (λ = 1.5418 Å) as the radiation source. Fourier transform infrared (FTIR) spectra were measured at room temperature in the 4000 to 350 cm-1 wave number range by PerkinElmer FTIR-300 spectrometer using the KBr pellet method. Field Emission Scanning Electron Microscope (FESEM) of Model INSPECTTM S50 was used for morphological studies. UV-Vis absorption spectra were measured using a Shimadzu UV-Visible spectrophotometer (UV-1800).

2.5. Photocatalytic degradation studies.

The photocatalytic degradation of phenol red (PR) in water was carried out at room temperature using a 300 ml photo reactor under UV irradiation. The UV source was a 125 W

mercury vapor lamp from Philips India, placed in a wooden box. An optimal catalyst loading of 0.8 g/L was used in the presence of 0.01 mmol of H_2O_2, and the pH of the solution was adjusted to 4.5. Different concentrations of phenol red (ranging from 10 to 1000 ppm) were selected for the investigation. Before exposing the sample solution to UV radiation, it was stirred in the dark for 30 minutes to achieve equilibrium between the components in the solution and atmospheric oxygen. For kinetic studies, 3 ml of the sample was collected at regular intervals and analyzed using a UV-Vis spectrophotometer in the range of 200 to 800 nm. The degradation of phenol red was monitored by observing changes in the absorption maximum at 432 nm using a calibration curve. The percentage of degradation was calculated by comparing the initial and final UV-Vis absorption measurements, as described below equation:

$$\% \text{ Degradation} = \frac{C_0 - C_t}{C_0} \text{ X } 100 \quad (1)$$

Where C_o= initial concentration of PR, Ct = concentration of PR after a certain duration of photoirradiation

3. Results and Discussion

3.1. X-ray diffraction study.

The structural analysis of both compounds, $Ca_2Fe_2O_5$ and the composite $Ca_2Fe_2O_5$-TiO_2 was conducted using the powder X-ray diffraction (PXRD) method, and the corresponding patterns are presented in Figure 2. The PXRD patterns of both samples, after being calcined at 900°C for 12 hours, clearly show the presence of the Brownmillerite phase of $Ca_2Fe_2O_5$ (JCPDS—Pattern 38-0408) [34] with an orthorhombic crystal system and *Pnma* space group. The d values for $Ca_2Fe_2O_5$ match well with those reported in the literature for this phase [35]. However, a minor impurity peak indicates the presence of Fe_3O_4 [36]. In the case of the composite $Ca_2Fe_2O_5$-TiO_2, the appearance of additional diffraction peaks corresponding to TiO_2 anatase confirms the successful synthesis of the composite, as depicted in Figure 2(B). XRD analysis confirms the formation of the desired crystalline structures of $Ca_2Fe_2O_5$ and the composite $Ca_2Fe_2O_5$-TiO_2 through the microwave-assisted hydrothermal method.

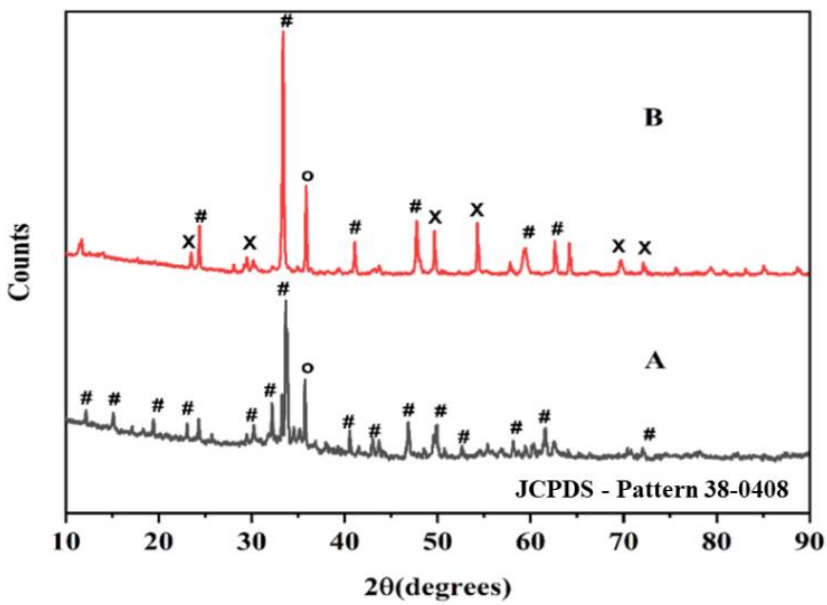

Figure 2. XRD patterns of **(A)** $Ca_2Fe_2O_5$; **(B)** $Ca_2Fe_2O_5$-TiO_2. (x, TiO_2; o, Fe_3O_4).

3.2. FTIR spectra analysis.

The formation of the compounds $Ca_2Fe_2O_5$ and $Ca_2Fe_2O_5$-TiO_2 was further confirmed through FTIR analysis. The FTIR spectra of both catalysts are depicted in Figure 3. The broad IR bands observed at approximately 3440 cm^{-1} and 1634 cm^{-1} correspond to the stretching and bending vibrations of OH groups, indicating the presence of adsorbed water molecules on the surface of the compounds during synthesis. Additionally, the peak observed at 1400-1460 cm^{-1} indicates the adsorption of CO_2 from the atmosphere on the catalyst surface.

In Figure 3(**A**), a sharp absorption band at ~567 cm^{-1} is observed, which can be attributed to the characteristic Fe-O stretching vibration of $Ca_2Fe_2O_5$. On the other hand, in Figure 3(**B**), the appearance of a peak at 590 cm^{-1} is due to the vibration of the Ti-O-O bond, along with the Fe-O stretching band at ~551 cm^{-1}. These observations confirm the successful formation of the $Ca_2Fe_2O_5$-TiO_2 composite and support the findings from the XRD analysis.

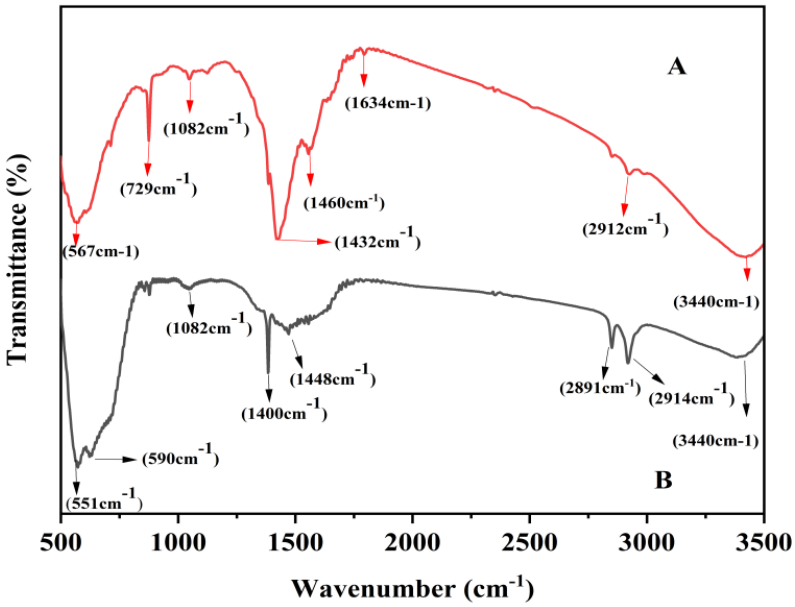

Figure 3. FTIR spectra of (**A**) $Ca_2Fe_2O_5$; (**B**) $Ca_2Fe_2O_5$-TiO_2.

3.3. Scanning electron microscopic studies.

The microstructures of the synthesized samples were examined using FESEM, and the micrographs of $Ca_2Fe_2O_5$ and the $Ca_2Fe_2O_5$-TiO_2 composite are presented in Figure 4. In Figure 4(**a**), the micrograph of $Ca_2Fe_2O_5$ reveals a dense flake-like morphology, with the particles highly agglomerated, possibly due to the magnetic nature of the compound. On the other hand, the micrograph of the $Ca_2Fe_2O_5$-TiO_2 composite (Figure 4(**b**)) clearly shows a combination of two distinct morphologies. The TiO_2 particles are seen to be dispersed on the flakes of $Ca_2Fe_2O_5$, forming a unique composite structure.

These different microstructures of the compounds are expected to impact their photocatalytic efficiency significantly. The well-defined morphologies and the synergistic effect between $Ca_2Fe_2O_5$ and TiO_2 in the composite material can enhance the photocatalytic performance, making it a promising catalyst for various environmental applications, including the degradation of pollutants in water.

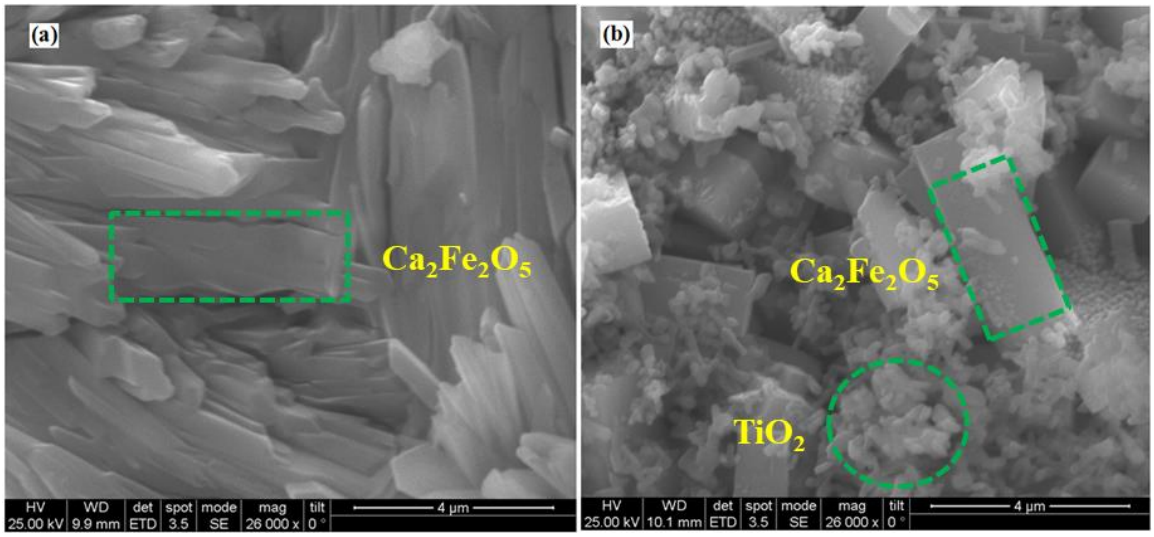

Figure 4. FESEM micrograph of (**a**) $Ca_2Fe_2O_5$; (**b**) $Ca_2Fe_2O_5$-TiO_2.

3.4. Band gap of the photocatalysts.

The optical band gap of a photocatalyst plays a critical role in its performance, and therefore, the optical properties of the compounds were investigated through UV-Vis absorption studies. $Ca_2Fe_2O_5$ displayed an absorption peak at around 350 nm (~3.7 eV), as shown in Figure 5(**A**) and (**B**). Notably, the $Ca_2Fe_2O_5$-TiO_2 composite exhibited a distinctly broader absorption peak. Upon deconvoluting the broad peak, two distinct peaks were identified at around 350 nm (~3.7 eV) and 426 nm (~2.91 eV), which can be attributed to the characteristic absorption of $Ca_2Fe_2O_5$ and TiO_2, respectively (Figure 5(**A**) and (**B**)). This indicates that the composite material comprises both $Ca_2Fe_2O_5$ and TiO_2 components.

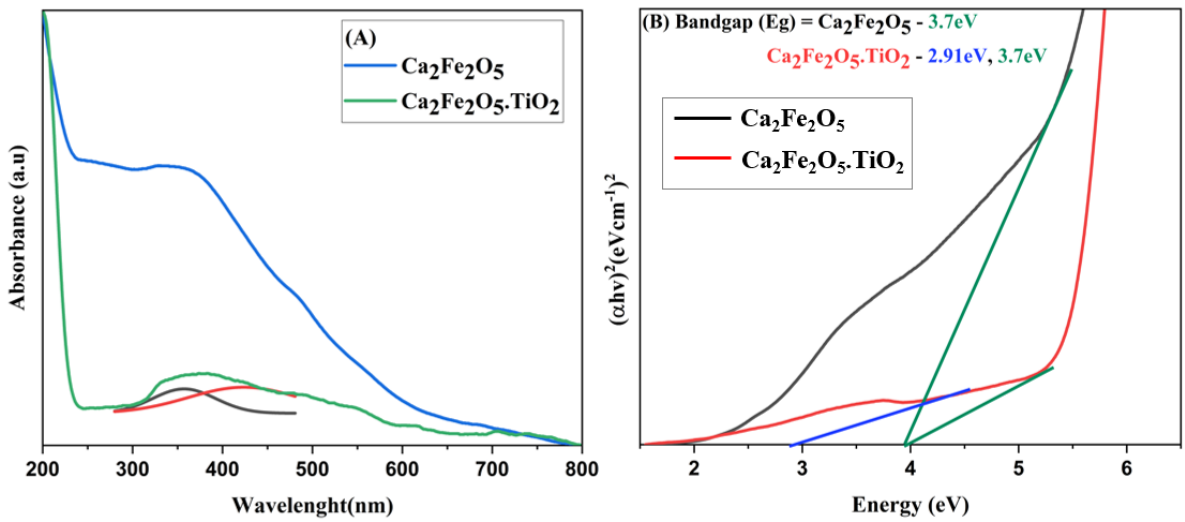

Figure 5. (**A**) UV-Vis absorption spectra; (**B**) Calculated band gap of $Ca_2Fe_2O_5$ and $Ca_2Fe_2O_5.TiO_2$.

These two distinct absorption peaks in the composite lead to a significant enhancement in the absorption range, spanning from 350nm to 426 nm in the UV region. This broadened absorption range is expected to enhance the photocatalytic degradation capability of the composite material under UV irradiation. Consequently, the composite $Ca_2Fe_2O_5$-TiO_2 shows promising potential as an efficient photocatalyst for various environmental applications, especially for water pollutants' degradation.

3.5. Photocatalytic degradation studies.

Effect of various parameters on photocatalytic efficiency:

3.5.1. Effect of pH on phenol red degradation.

The pH of the solution is a crucial parameter in photocatalytic reactions occurring on catalyst surfaces, as it directly impacts the surface charge properties of the photocatalyst. Phenol red exists in three different forms depending on the pH of the solution. At low and high pH, it exists as a negatively charged molecule; at moderate pH, it exists as a zwitterion, as illustrated in Figure 6.

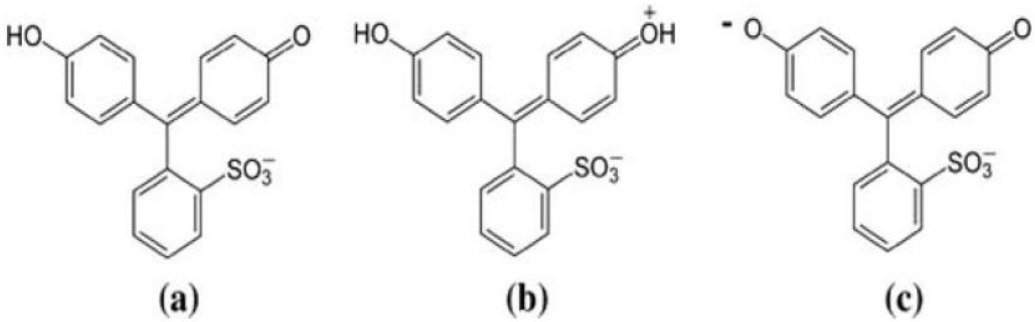

Figure 6. Molecular structure of phenol red at different pH **(a)** low pH; **(b)** moderate pH; **(c)** high pH.

Since phenol red dye is negatively charged at low pH, the catalyst surface is positively charged, which facilitates higher adsorption of the dye on the surface due to electrostatic attraction. On the other hand, at higher pH levels, the number of negatively charged sites on the surface increases, and the number of positively charged sites declines, resulting in a decrease in adsorption due to repulsion between the dye and the negatively charged catalyst surface. Hence, optimizing the pH is essential for any photocatalytic degradation process.

The present study conducted phenol red degradation experiments over a pH range of 2 to 8, with an optimum catalyst dosage of 0.08 g and an initial dye concentration of 10 ppm. The results showed that phenol red degradation was most favorable at a mildly acidic pH of 4.5, as shown in Table 1. Based on this finding, a pH of 4.5 was considered the optimum condition for the photocatalytic degradation of phenol red(Figure 6)

3.5.2. Effect of catalyst loading.

The amount of catalyst used in the photocatalytic degradation process plays a crucial role in determining the efficiency of the reaction. It affects the number of active sites available for the reaction and impacts the catalyst's overall photocatalytic ability. This study investigated the photodegradation of phenol red using different amounts of catalyst, ranging from 0.03 to 0.1 g, and found that 0.08 g of catalyst was the optimal amount to achieve the maximum reaction rate. Beyond this optimum amount, an increase in the catalyst quantity had a negative effect on the photocatalytic degradation of phenol red and observed a drop in the photodegradation efficiency, which can be attributed to the aggregation of catalyst particles leading to increased opacity and light scattering. This aggregation may reduce the availability of active sites and hinder the effective interaction between the catalyst and the pollutant, thereby decreasing the degradation efficiency. At the optimal catalyst amount of 0.08 g, 100% phenol red degradation was achieved, as depicted in Table 1, confirming the effectiveness of this specific catalyst dosage for the photocatalytic degradation process.

Table 1. Optimization of phenol red degradation under UV light irradiation with $Ca_2Fe_2O_5$ photocatalysts.

©	Phenol red (ppm)	Catalyst (mg)	H_2O_2 (mmol)	pH	Time (h)	Degradation (%)
1	10	30	Absence	11.5	3	36
2	10	50	Absence	11.5	3	38
3	10	50	5×10^{-3}	11.5	1.5	68
4	10	50	5×10^{-3}	6	1.5	79
5	10	50	5×10^{-3}	5	1.5	81
6	10	50	1×10^{-2}	4.5	1	86
7	10	80	1×10^{-2}	4.5	0.5	100
8	10	80	1×10^{-2}	3.0	0.5	84
9	10	80	2×10^{-2}	4.5	0.5	89
10	10	100	1×10^{-2}	4.5	2	74

3.5.3. Effect of H_2O_2.

The recombination of electrons and holes (e^-/h^+) is a significant challenge in photocatalytic studies. To address this issue, Malato [35] and his colleagues have explored the use of electron acceptors to inhibit e^-/h^+ recombination. The present study conducted photocatalytic reactions both with and without the addition of hydrogen peroxide (H_2O_2) as an electron acceptor.

It was observed that in the absence of H_2O_2, only 38% of phenol red degradation occurred over the $Ca_2Fe_2O_5$ catalyst. However, when H_2O_2 was present in the reaction medium, the photodegradation yield significantly improved, reaching 100%. The addition of H_2O_2 effectively hindered e^-/h^+ recombination, leading to enhanced photocatalytic degradation of phenol red.

It is worth noting that excessive amounts of H_2O_2 did not further enhance the photocatalytic degradation, and instead, it resulted in a decrease in phenol red degradation efficiency (as shown in Table 1). This observation suggests that the optimal amount of H_2O_2 is crucial for achieving maximum photocatalytic efficiency and further emphasizes the importance of balancing electron acceptor concentration in the reaction medium.

3.5.4. Degradation of phenol red from aqueous solutions using $Ca_2Fe_2O_5$ photocatalyst in the presence of H_2O_2 under UV irradiation.

The photocatalytic experiments were conducted under UV light irradiation using various concentrations of phenol red (10, 30, 50, 100, 150, and 200 ppm) with the optimized reaction conditions over the $Ca_2Fe_2O_5$ catalyst (catalyst 0.08 g, pH 4.5, and H_2O_2 0.01 mmol).

Table 2. Percentage of phenol red (PR) degradation and rate constant over the $Ca_2Fe_2O_5$ photocatalyst under UV irradiation.

S. No.	Conc. of PR (ppm)	Conc. of H_2O_2 (mmol.)	Duration (h)	PR degradation (%)	Rate constant k (min^{-1})
1	10	$1x10^{-2}$	0.5	100	$3.13x10^{-2}$
2	30	$1x10^{-2}$	1	100	$5.04x10^{-3}$
3	50	$1x10^{-2}$	2	100	$5.72x10^{-3}$
4	80	$1x10^{-2}$	3.5	99	$9.82x10^{-3}$
5	100	$1x10^{-2}$	4	94	$7.51x10^{-3}$
6	120	$1x10^{-2}$	6	62	-
7	150	$1x10^{-2}$	6	47	-
8	200	$1x10^{-2}$	6	36	-

To establish control, blank tests were also performed by irradiating phenol red aqueous solution alone without the catalyst for one and a half hours, with samples collected at 15-minute

intervals to monitor any changes. However, no significant degradation was observed in the blank tests, indicating that the organic compound in the solution was stable under UV light even after one and a half hours of irradiation.

The photodegradation profiles of phenol red over the $Ca_2Fe_2O_5$ photocatalyst under UV irradiation at different concentrations of phenol red and with the optimized conditions (catalyst 0.08 g, pH 4.5, and H_2O_2 0.01 mmol) are shown in Figure 7(A), and the corresponding degradation efficiencies are presented in Table 2. As time progressed, the concentration of phenol red in the water decreased and eventually approached zero, indicating 100% removal of phenol red from the water over the $Ca_2Fe_2O_5$ catalyst. The results demonstrate efficient phenol red degradation over the $Ca_2Fe_2O_5$ catalyst in a relatively short duration. However, at higher concentrations (> 100 ppm), the degradation efficiency decreased, which could be attributed to blocking active sites by previously adsorbed phenol red molecules.

The kinetics of phenol red degradation (in Figure 8) followed the first-order kinetics as given below.

$$\ln (C_t/C_0) = -kt \quad (2)$$

Where C0 and Ct denote the initial concentration of phenol red and the concentration at UV illumination time t (h), respectively, and k (h−1) represents the rate constant of the first-order reaction. The first-order rate constant k values were derived from the slope of the curve obtained by plotting −ln(Ct/C0) against time for various concentrations (refer to Figure 7). The determined k values are presented in Table 2 and are found to be 3.13×10^{-2}, 5.04×10^{-3}, 5.72×10^{-3}, $9.82 \times 10^{-3}$and 7.51×10^{-3} for the degradation of 10, 30, 50, 80, 100 ppm of phenol red respectively with the $Ca_2Fe_2O_5$ photocatalyst.

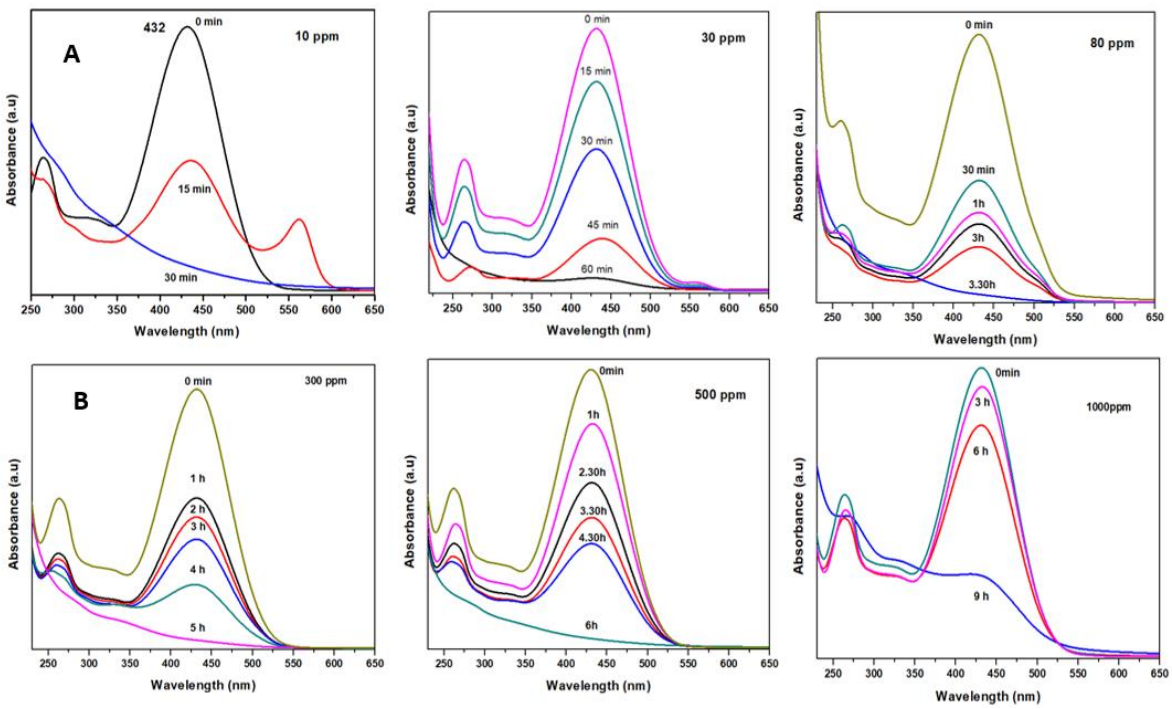

Figure 7. Representative UV-Vis degradation profiles of phenol red with respect to time on (**A**) $Ca_2Fe_2O_5$; (**B**) $Ca_2Fe_2O_5$– TiO_2 photocatalysts.

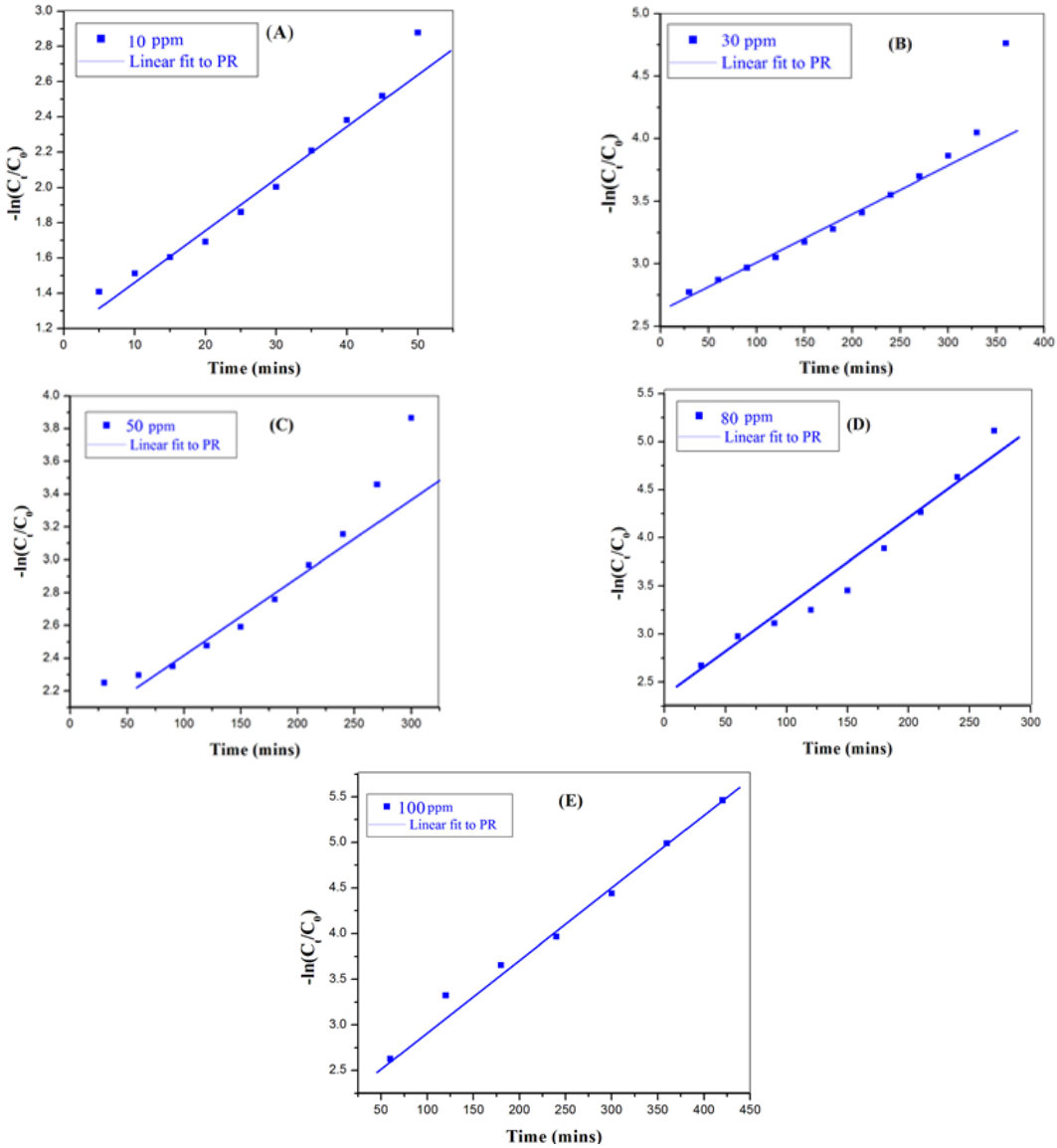

Figure 8. First-order kinetics of **(A)** 10 ppm; **(B)** 30 ppm; **(C)** 50 ppm; **(D)** 80 ppm; **(E)** 100 ppm of phenol red degradation as a function of time with $Ca_2Fe_2O_5$ photocatalyst.

3.5.5. Degradation of phenol red with $Ca_2Fe_2O_5$–TiO_2 composite with H_2O_2 under UV irradiation.

The photocatalytic degradation of phenol red was studied under UV light irradiation using the $Ca_2Fe_2O_5$–TiO_2 catalyst with the addition of H_2O_2 at various concentrations (100-1000 ppm), as shown in Table 3. The degradation profiles for selected concentrations are illustrated in Figure 7(B). Substantial changes were observed in the absorption maximum at 432 nm over time, indicating a complete degradation of phenol red (100% degradation). Table 3 shows that the $Ca_2Fe_2O_5$–TiO_2 catalyst exhibited 100-74% degradation of phenol red within 2.5 to 9 hours for concentrations of 100, 200, 300, 500, 800, and 1000 ppm.

The rate constants (k) for the reactions were determined from the slope of the curve obtained when $-\ln(C_t/C_0)$ was plotted against time for various concentrations (Figure 8). The calculated k values for the degradation of 100, 200, 300, and 500 ppm of phenol red with the $Ca_2Fe_2O_5$–TiO_2 photocatalyst were found to be 2.18×10^{-2}, 1.08×10^{-2}, 6.41×10^{-3}, and 6.16×10^{-3} h^{-1}, respectively. These results demonstrate the efficient and rapid degradation of phenol red by the $Ca_2Fe_2O_5$–TiO_2 photocatalyst.

Table 3. Percentage of phenol red (PR) degradation and rate constant over the $Ca_2Fe_2O_5$-TiO_2 nanocomposite photocatalyst under UV irradiation.

S. No.	Conc. of PR (ppm)	Conc. H_2O_2 (mmol.)	Duration (h)	PR degradation (%)	Rate constant k (min^{-1})
1	100	$1x10^{-2}$	2.5	100	$2.18x10^{-2}$
2	200	$1x10^{-2}$	3.5	100	$1.08x10^{-2}$
3	300	$1x10^{-2}$	5	100	$6.41x10^{-3}$
4	500	$1x10^{-2}$	6	100	$6.16x10^{-3}$
5	800	$1x10^{-2}$	9	90	-
6	1000	$1x10^{-2}$	9	74	-

3.5.6. Mechanistic studies of degradation of phenol red.

The results of the present study demonstrate that the photocatalytic efficiency can be significantly improved by adding hydrogen peroxide to the reaction mixture in combination with $Ca_2Fe_2O_5$ and $Ca_2Fe_2O_5$-TiO_2 (as shown in Figure 9). The presence of H_2O_2 plays a crucial role in the photocatalytic process, as there is a direct relationship between the concentration of H_2O_2 and the degradation of phenol red. The photocatalytic degradation increases with higher concentrations of H_2O_2 due to its electron acceptor nature, consistent with previous research findings [37-39].

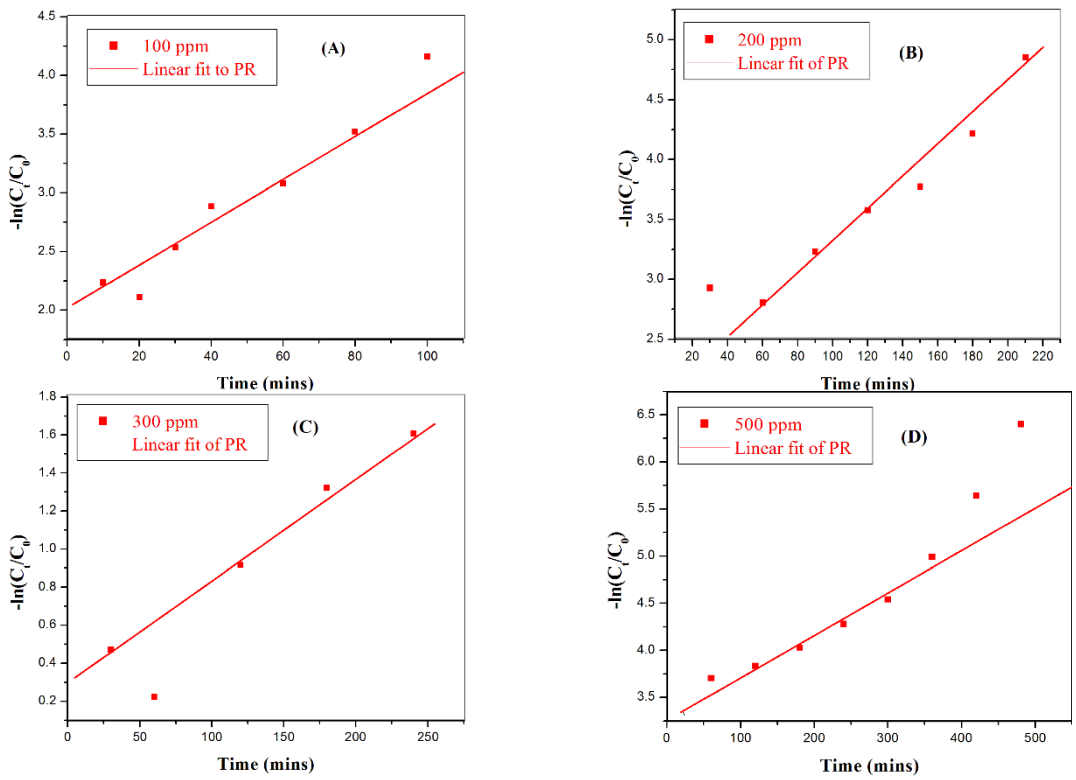

Figure 9. First-order kinetics of **(A)** 100 ppm; **(B)** 200 ppm; **(C)** 300 ppm; **(D)** 1000 ppm of phenol red degradation as a function of time with $Ca_2Fe_2O_5$–TiO_2 photocatalyst.

The beneficial effect of H_2O_2 addition can be explained in two ways: firstly, the production of additional OH radicals, which have a standard redox potential of +2.8 V, act as strong oxidizing agents under UV light radiation [40]. These OH radicals play a key role in degrading phenol red and other organic pollutants. Secondly, the presence of H_2O_2 enhances the separation of electron-hole pairs generated during the photocatalytic process, thus reducing the recombination of these charge carriers, which would otherwise limit the photocatalytic efficiency [41]. The combination of $Ca_2Fe_2O_5$ and TiO_2 in the composite further enhances the

photocatalytic performance, leading to rapid and efficient degradation of phenol red under UV irradiation in the presence of H_2O_2. The general mechanism is shown below:

$Ca_2Fe_2O_5 + h\nu(UV) \longrightarrow e_{CB}^- + h_{VB}^+$

$h_{VB}^+ + H_2O \longrightarrow H^+ + {}^{\cdot}OH$

$e_{CB}^- + O_2 \longrightarrow O_2^{\cdot -}$

$H_2O_2 + e_{CB}^- \longrightarrow {}^{\cdot}OH + OH^-$

$H_2O_2 + h\nu \longrightarrow {}^{\cdot}OH + {}^{\cdot}OH$

$H_2O_2 + O_2^{\cdot -} \longrightarrow {}^{\cdot}OH + OH^- + O_2$

(b) inhibition of e^-/h^+ recombination can be explained in terms of catalyst surface modification via H_2O_2 adsorption and scavenging of photoproduced holes by the following reaction:

$H_2O_2 + 2h_{VB}^+ \longrightarrow O_2 + 2H^+$

Hydroxyl radicals decompose the dye into simpler ions/molecules such as carbon dioxide, water, sulfur dioxide, etc.

Phenol red + ${}^{\cdot}OH \longrightarrow$ Products

${}^{\cdot}OH + {}^{\cdot}OH \longrightarrow H_2O_2$

$H_2O_2 \longrightarrow 2H_2O + O_2$

Therefore, the reactions described above suggest that UV/Catalyst/H_2O_2 systems are likely to generate more hydroxyl radicals, along with the potential appearance of other oxidizing species during the electron/hole generation process.

3.5.7. Comparison of the results with previous studies.

Comparing the present study with previous reports on the photocatalytic degradation of phenol red, some notable differences and advantages can be observed. Table 4 shows that most of the previous studies used lower concentrations of phenol red for photocatalytic degradation, and their degradation efficiencies were generally lower compared to the results obtained in the present study. The present study uses a wide range of phenol red concentrations (ranging from 10 to 1000 ppm) in water for degradation.

Remarkably, the UV/H_2O_2/$Ca_2Fe_2O_5$-TiO_2 system achieved 100% degradation efficiency for concentrations between 100 and 500 ppm of phenol red and still showed a high % degradation efficiency of 74% for concentrations of 800 and 1000 ppm. These results are significant and demonstrate the effectiveness of the $Ca_2Fe_2O_5$-TiO_2 composite in efficiently degrading high concentrations of phenol red in aqueous solutions.

The high potential of the $Ca_2Fe_2O_5$-TiO_2 system as an industrial catalyst for the removal of dye effluents from wastewater is highlighted by these results. The ability to achieve such high degradation efficiencies for a wide range of concentrations indicates the promising application of this photocatalytic system for treating industrial wastewater containing high concentrations of dye pollutants. The UV/H_2O_2/$Ca_2Fe_2O_5$-TiO_2 system can be a cost-effective and environmentally friendly solution for the treatment of dye-contaminated wastewater in various industries. The study's findings contribute to the growing interest in using advanced nanocomposite photocatalysts for effective water treatment and environmental remediation.

Table 4. Comparison of photocatalytic activity of the present studies with the reported systems.

Catalyst	PR Conc. (ppm)	Type of Radiation	Degradation (%)	References
$Ca_2Fe_2O_5$	10-100	UV	100-94	Present study
$Ca_2Fe_2O_5$-TiO_2	10-500	UV	100	Present study
	800-1000		90-74	
Ni-doped Niobia/carbon composite	12.5	UV	82	[41]
$BiLaFeO_3$	3.5	Visible	90	[42]
$NiMn_2O_4$	18	UV	98	[43]
Fe (III) Goethite	3.54	Solar light	98	[44]
TiO_2 nanoparticles	10	UV	94	[45]

4. Conclusion

The synthesis of $Ca_2Fe_2O_5$ and $Ca_2Fe_2O_5$-TiO_2 photocatalysts was successfully prepared via the microwave-assisted hydrothermal method. Characterization revealed band gap energies of 2.48 eV for $Ca_2Fe_2O_5$ and 3.64 eV for $Ca_2Fe_2O_5$-TiO_2, with X-ray diffraction confirming the presence of the brownmillerite phase in both materials. Morphological analysis using FE-SEM indicated a flake-like structure for $Ca_2Fe_2O_5$ and a combination of particle and flake-like morphology for $Ca_2Fe_2O_5$-TiO_2.

The photocatalytic activity of these materials was assessed for phenol red dye degradation across concentrations ranging from 10 ppm to 1000 ppm under optimized conditions: 0.01 mmol H_2O_2, pH 4.5, and 0.08 g catalyst. Degradation efficiencies ranged from 100% to 74% for both materials, with $Ca_2Fe_2O_5$-TiO_2 exhibiting superior performance, particularly at high dye concentrations, attributed to TiO_2 presence enhancing degradation capacity.

Phenol red degradation kinetics followed first-order reactions for both photocatalysts. These findings underscore the potential of the $Ca_2Fe_2O_5$-TiO_2 composite as a cost-effective nanomaterial for industrial wastewater treatment, offering enhanced photocatalytic properties and efficient organic pollutant degradation, thus finding applications in environmental remediation and water treatment.

Funding

This work was financially supported by the University Grants Commission (UGC) India.

Acknowledgments

The authors express gratitude to the University Grants Commission (UGC) India for providing financial support

Conflicts of Interest

The authors declare no conflict of interest.

References

1. Hoffmann, M.R.; Martin, S.T.; Choi, W.; Bahnemann, D.W. Environmental Applications of Semiconductor Photocatalysis. *Chem. Rev.* **1995**, *95*, 69-96, https://doi.org/10.1021/cr00033a004.
2. Carp, O.; Huisman, C.L.; Reller, A. Photoinduced reactivity of titanium dioxide. *Prog. Solid State Chem.* **2004**, *32*, 33-177, https://doi.org/10.1016/j.progsolidstchem.2004.08.001.

3. Thu, H.B.; Karkmaz, M.; Puzenat, E.; Guillard, C.; Herrmann, J.-M. From the fundamentals of photocatalysis to its applications in environment protection and in solar purification of water in arid countries. *Res. Chem. Intermed.* **2005**, 31, 449-461, https://doi.org/10.1163/1568567053956671.
4. Kubacka, A.; Fernández-García, M.; Colón, G. Advanced Nanoarchitectures for Solar Photocatalytic Applications. *Chem. Rev.* **2012**, *112*, 1555-1614, https://doi.org/10.1021/cr100454n.
5. Srilakshmi, C.; Saraf, R.; Prashanth, V.; Rao, G.M.; Shivakumara, C. Structure and Catalytic Activity of Cr-Doped $BaTiO_3$ Nanocatalysts Synthesized by Conventional Oxalate and Microwave Assisted Hydrothermal Methods. *Inorg. Chem.* **2016**, *55*, 4795-4805, https://doi.org/10.1021/acs.inorgchem.6b00240.
6. Yu, K.; Yang, S.; Liu, C.; Chen, H.; Li, H.; Sun, C.; Boyd, S.A. Degradation of Organic Dyes via Bismuth Silver Oxide Initiated Direct Oxidation Coupled with Sodium Bismuthate Based Visible Light Photocatalysis. *Environ. Sci. Technol.* **2012**, *46*, 7318-7326, https://doi.org/10.1021/es3001954.
7. Shaterian, M.; Enhessari, M.; Rabbani, D.; Asghari, M.; Salavati-Niasari, M. Synthesis, characterization and photocatalytic activity of $LaMnO_3$ nanoparticles. *Appl. Surf. Sci.* **2014**, *318*, 213-217, https://doi.org/10.1016/j.apsusc.2014.03.087.
8. Qu, Y.; Zhou, W.; Ren, Z.; Du, S.; Meng, X.; Tian, G.; Pan, K.; Wang, G.; Fu, H. Facile preparation of porous $NiTiO_3$ nanorods with enhanced visible-light-driven photocatalytic performance. *J. Mater. Chem.* **2012**, *22*, 16471-16476, https://doi.org/10.1039/c2jm32044d.
9. Devi, L.G.; Krishnamurthy, G. TiO_2- and $BaTiO_3$-Assisted Photocatalytic Degradation of Selected Chloroorganic Compounds in Aqueous Medium: Correlation of Reactivity/Orientation Effects of Substituent Groups of the Pollutant Molecule on the Degradation Rate. *J. Phys. Chem. A* **2011**, *115*, 460-469, https://doi.org/10.1021/jp103301z.
10. Zaki, M.I.; Ramadan, W.; Katrib, A.; Rabee, A.I.M. Surface chemical and photocatalytic consequences of Ca-doping of $BiFeO_3$ as probed by XPS and H_2O_2 decomposition studies. *Appl. Surf. Sci.* **2014**, *317*, 929-934, https://doi.org/10.1016/j.apsusc.2014.09.007.
11. Tijare, S.N.; Joshi, M.V.; Padole, P.S.; Mangrulkar, P.A.; Rayalu, S.S.; Labhsetwar, N.K. Photocatalytic hydrogen generation through water splitting on nano-crystalline $LaFeO_3$ perovskite. *Int. J. Hydrog. Energy* **2012**, *37*, 10451-10456, https://doi.org/10.1016/j.ijhydene.2012.01.120.
12. Pecchi, G.; Campos, C.; Peña, O. Thermal stability against reduction of $LaMn_{1-y}Co_yO_3$ perovskites. *Mater. Res. Bull.* **2009**, *44*, 846-853, https://doi.org/10.1016/j.materresbull.2008.09.009.
13. Yang, Y.; Sun, Y.; Jiang, Y. Structure and photocatalytic property of perovskite and perovskite-related compounds. *Mater. Chem. Phys.* **2006**, *96*, 234-239, https://doi.org/10.1016/j.matchemphys.2005.07.007.
14. Rizzo, L.; Koch, J.; Belgiorno, V.; Anderson, M.A. Removal of methylene blue in a photocatalytic reactor using polymethylmethacrylate supported TiO_2 nanofilm. *Desalination* **2007**, *211*, 1-9, https://doi.org/10.1016/j.desal.2006.02.081.
15. hiyong, Y.; Mielczarski, E.; Mielczarski, J.; Laub, D.; Buffat, P.; Klehm, U.; Albers, P.; Lee, K.; Kulik, A.; Kiwi-Minsker, L.; Renken, A.; Kiwi, J. Preparation, stabilization and characterization of TiO_2 on thin polyethylene films (LDPE). Photocatalytic applications. *Water Res.* **2007**, *41*, 862-874, https://doi.org/10.1016/j.watres.2006.11.020.
16. Dunlop, P.S.M.; Galdi, A.; McMurray, T.A.; Hamilton, J.W.J.; Rizzo, L.; Byrne, J.A. Comparison of Photocatalytic Activities of Commercial Titanium Dioxide Powders Immobilised on Glass Substrates. *J. Adv. Oxid. Technol.* **2010**, *13*, 99-106, https://doi.org/10.1515/jaots-2010-0113.
17. Pavasupree, S.; Suzuki, Y.; Pivsa-Art, S.; Yoshikawa, S. Preparation and characterization of mesoporous TiO_2–CeO_2 nanopowders respond to visible wavelength. *J. Solid State Chem.* **2005**, *178*, 128-134, https://doi.org/10.1016/j.jssc.2004.10.028.
18. Li, G.; Zhang, D.; Yu, J.C. Thermally stable ordered mesoporous CeO_2/TiO_2 visible-light photocatalysts. *Phys. Chem. Chem. Phys.* **2009**, *11*, 3775-3782, https://doi.org/10.1039/B819167K.
19. Liu, H.; Wang, M.; Wang, Y.; Liang, Y.; Cao, W.; Su, Y. Ionic liquid-templated synthesis of mesoporous CeO_2–TiO_2 nanoparticles and their enhanced photocatalytic activities under UV or visible light. *J. Photochem. Photobiol. A: Chem.* **2011**, *223*, 157-164, https://doi.org/10.1016/j.jphotochem.2011.06.014.
20. Wang, Y.; Li, B.; Zhang, C.; Cui, L.; Kang, S.; Li, X.; Zhou, L. Ordered mesoporous CeO_2-TiO_2 composites: Highly efficient photocatalysts for the reduction of CO_2 with H_2O under simulated solar irradiation. *Appl. Catal. B: Environ.* **2013**, *130-131*, 277-284, https://doi.org/10.1016/j.apcatb.2012.11.019.
21. Zhou, L.; Gao, C.; Xu, W. Magnetic Dendritic Materials for Highly Efficient Adsorption of Dyes and Drugs. *ACS Appl. Mater. Interfaces* **2010**, *2*, 1483-1491, https://doi.org/10.1021/am100114f.

22. Shenoy, S.; Chuaicham, C.; Okumura, T.; Sekar, K.; Sasaki, K. Simple tactic polycondensation synthesis of Z-scheme quasi-polymeric g-C_3N_4/$CaFe_2O_4$ composite for enhanced photocatalytic water depollution *via* p-n heterojunction. *Chem. Eng. J.* **2023**, *453*, 139758, https://doi.org/10.1016/j.cej.2022.139758.
23. Sharma, R.; Mandyal, P.; Sambyal, S.; Fang, B.; Kumar, V.; Gholami, P.; Priye, A.; Shandilya, P. Fundamentals and Functional Mechanisms of Photocatalysis in Water Treatment. In Photocatalysts and Electrocatalysts in Water Remediation, Bhunia, P., Dutta, K., Vadivel, S., Eds.; John Wiley & Sons Ltd, **2022**; 1-37, https://doi.org/10.1002/9781119855347.ch1.
24. Lima, C.G.M.; Araújo, A.J.M.; Silva, R.M.; Raimundo, R.A.; Grilo, J.P.F.; Constantinescu, G.; Kovalevsky, A.V.; Macedo, D.A. Electrical assessment of brownmillerite-type calcium ferrite materials obtained by proteic sol-gel route and by solid-state reaction using mollusk shells. *J. Solid State Chem.* **2021**, *299*, 122172, https://doi.org/10.1016/j.jssc.2021.122172.
25. Kamali, M.; Sheibani, S.; Ataie, A. Effect of calcination temperature on photocatalytic activity of magnetic Fe-based composites recycled from hazardous EAF dust. *Mater. Res. Bull.* **2022**, *148*, 111688, https://doi.org/10.1016/j.materresbull.2021.111688.
26. Konicki, W.; Sibera, D.; Mijowska, E.; Lendzion-Bieluń, Z.; Narkiewicz, U. Equilibrium and kinetic studies on acid dye Acid Red 88 adsorption by magnetic $ZnFe_2O_4$ spinel ferrite nanoparticles. *J. Colloid Interface Sci.* **2013**, *398*, 152-160, https://doi.org/10.1016/j.jcis.2013.02.021.
27. Zaggout, F.R. Entrapment of phenol red pH indicator into a sol–gel matrix. *Mater. Lett.* **2006**, *60*, 1026-1030, https://doi.org/10.1016/j.matlet.2005.10.100.
28. Almulhem, N.; Awada, C.; Shaalan, N.M. Photocatalytic Degradation of Phenol Red in Water on Nb(x)/TiO_2 Nanocomposites. *Crystals* **2022**, *12*, 911, https://doi.org/10.3390/cryst12070911.
29. Mousavi, S.M.; Meraji, S.H.; Sanati, A.M.; Ramavandi, B. Phenol red dye removal from wastewater using TiO_2-FSM-16 and Ni-FSM-16 photocatalysts. *Heliyon* **2023**, *9*, e14488, https://doi.org/10.1016%2Fj.heliyon.2023.e14488.
30. Almulhem, N.K.; Awada, C.; Shaalan, N.M. Study of Phenol Red Photocatalytic Decomposition on $KBrO_3$-Supported TiO_2 Nanoparticles for Wastewater Treatment. *Separations* **2023**, *10*, 162, https://doi.org/10.3390/separations10030162.
31. Ahlawat, A.; Dhiman, T.K.; Solanki, P.R.; Rana, P.S. Enhanced Photocatalytic Degradation of *p*-Nitrophenol and Phenol Red Through Synergistic Effects of a CeO_2-TiO_2 Nanocomposite. *Catal. Res.* **2022**, *2*, 039, https://doi.org/10.21926/cr.2204039.
32. Yang, X.; Chen, W.; Huang, J.; Zhou, Y.; Zhu, Y.; Li, C. Rapid degradation of methylene blue in a novel heterogeneous Fe_3O_4@ rGO@ TiO_2-catalyzed photo-Fenton system. *Sci. Rep.* **2015**, *5*, 10632, https://doi.org/10.1038/srep10632.
33. Lan, H.; He, W.; Wang, A.; Liu, R.; Liu, H.; Qu, J.; Huang, C.P. An activated carbon fiber cathode for the degradation of glyphosate in aqueous solutions by the Electro-Fenton mode: Optimal operational conditions and the deposition of iron on cathode on electrode reusability. *Water Res.* **2016**, *105*, 575-582, https://doi.org/10.1016/j.watres.2016.09.036.
34. He, Y.; He, C.; Wang, F.; Guo, X.; Zhao, Z.; Zhang, X.; Chen, X.; Liu, X. Efficient degradation of Congo red and phenol by a new photocatalyst Ag/AgBr-Al-attapulgite composite under visible light irradiation. *Environ. Sci. Pollut. Res.* **2021**, *28*, 33320-33330, https://doi.org/10.1007/s11356-021-12737-9.
35. Da Silva, C.C.; Sombra, A.S.B. Temperature Dependence of the Magnetic and Electric Properties of $Ca_2Fe_2O_5$. *Mater. Sci. Appl.* **2011**, *2*, 1349-1353, https://doi.org/10.4236/msa.2011.29183.
36. The, C.M.; Mohamed, A.R. Roles of titanium dioxide and ion-doped titanium dioxide on photocatalytic degradation of organic pollutants (phenolic compounds and dyes) in aqueous solutions: A review. *J. Alloys Compd.* **2011**, *509*, 1648-1660, https://doi.org/10.1016/j.jallcom.2010.10.181.
37. Minyaylova, I.G.; Presnyakov, I.A.; Pokholok, K.V.; Sobolev, A.V.; Baranov, A.V.; Demazeau, G.; Govor, G.A.; Vetcher, A.K. Hyperfine Interactions and Dynamic Characteristics of ^{119}Sn Dopant Atoms in $Ca_2Fe_2O_5$. *J. Solid State Chem.* **2000**, *151*, 313-316, https://doi.org/10.1006/jssc.2000.8660.
38. Molinar-Díaz, J.; Woodliffe, J.L.; Steer, E.; Morley, N.A.; Brown, P.D.; Ahmed, I. Optimisation of the Flame Spheroidisation Process for the Rapid Manufacture of Fe_3O_4- Based Porous and Dense Microspheres. *Molecules* **2023**, *28*, 2523, https://doi.org/10.3390/molecules28062523.
39. Tenri Ola, A.T.; Rahmat, R.; Fahri, A.N.; Heryanto, H.; Mutmainna, I.; Sesa, E.; Tahir, D. Synergistic Effect of Chitosan and Activated Carbon (AC) in Suppressing Recombination Charge of Composite $Ca_2Fe_2O_5$⁻AC/Chitosan for High Photodegradation of Fipronil Wastewater. *J. Polym. Environ.* **2022**, *30*, 3218-3229, https://doi.org/10.1007/s10924-022-02425-1.

40. Rajakumar, G.; Rahuman, A.A.; Roopan, S.M.; Khanna, V.G.; Elango, G.; Kamaraj, C.; Zahir, A.A.; Velayutham, K. Fungus-mediated biosynthesis and characterization of TiO_2 nanoparticles and their activity against pathogenic bacteria. *Spectrochim. Acta - A: Mol. Biomol. Spectrosc.* **2012**, *91*, 23-29, https://doi.org/10.1016/j.saa.2012.01.011.
41. Agustina, M.; Linggawati, A.; Arifin, K. Cos as Co-Catalyst for Enhancing the TiO_2 Photoelectrochemical Water Splitting. *J. Phys.: Conf. Ser.* **2019**, *1351*, 012034, https://doi.org/10.1088/1742-6596/1351/1/012034.